Sensors & Transducers, Vol. 263, Issue 4, December 2023, pp. 1-11

www.sensorsportal.com

Sensors & Transducers
Published by IFSA Publishing, S. L., 2023
http://www.sensorsportal.com

Sensing the Mechanical Properties of AlN Thin Films Using Micromechanical Membranes in Combination with Finite-element Simulations

[1, 2, 3, *] **Menno POOT**
[1] Department of Physics, TUM School of Natural Sciences, Technical University of Munich, 85748 Garching, Germany
[2] Munich Center for Quantum Science and Technology (MCQST), 80799 Munich, Germany
[3] Institute for Advanced Study, Technical University of Munich, 85748 Garching, Germany
[1] Tel.: +49 89 289 12358, fax: +49 89 289 12536
E-mail: menno.poot@tum.de

Received: 15 September 2023 / Accepted: 16 December 2023 / Published: 21 December 2023

Abstract: The current interest in quantum technologies calls for the development of novel materials and hybrid structures. Understanding the mechanical properties of a material can be a challenge, especially at the nanoscale. We use the eigenfrequencies of in-house fabricated silicon nitride membranes in combination with finite-element simulations to extract the stress in a film that is deposited on top. The high stress results in sharp resonances that can be located precisely so that the mechanical properties of the top layer can be determined accurately. We highlight this approach using aluminum nitride – an important material for on-chip quantum optics and optomechanics – grown onto these micromechanical membranes. The detection is done optomechanically by exciting the modes using a piezo actuation and detecting the vibrations in the reflected laser light. For this, different lasers are at our disposal. The resonances of a wide variety of highly stressed membranes are measured. The frequencies follow the expected inverse length dependence of a stressed membrane and depend on the thickness of the top layer. To connect the experimental observations to the material properties, finite-element simulations are used. It is shown that full simulations of the membranes are only possible for simplified geometries. When simulating the actual geometry, this, however, becomes infeasible. It is shown that simulations of a single unit cell – in particular band structure calculations – can be used to accurately model the actual structure of the membrane. Although this approach is strictly speaking only valid for infinitely large membranes, it is shown that edge effects are negligible. With the simulations, the stress in the bilayer is determined. A cross-over between compressive and tensile stress is observed as a function of the AlN thickness.

Keywords: Optomechanics, Film stress, Aluminum nitride (AlN), MEMS, Silicon Nitride (SiN), Bilayer membrane, Finite-Element Simulations (FEM), Mechanical band structure.

1. Introduction

Micromechanical membranes provide an important platform for a wide variety of optomechanical experiments. This can range from scanning force microscopy [1], to study cavity optomechanical backaction [2], the observation of hybridization of degenerate eigenmodes [3], topological energy transfer [4], all the way to radiative heat transfer mediated via Casimir fluctuations [5]. Another important aspect of these very thin membranes is that they can be used to sense materials that are placed on top [6, 7]. This provides an interesting route to measuring the mechanical

properties of a variety of materials that can be deposited or grown on top of existing high-stress silicon nitride (SiN) membranes [8].

As will be described in detail in [8], we make membranes with and without the second layer on top and measure their eigenmodes. The dimensions of our membranes can be varied by design and typical sizes are 10s to 100s of µm in width and length. The thickness is determined by the SiN film thickness and is typically 100s of nm [3]. We illustrate that we can determine the stress in an aluminum nitride (AlN) layer grown on top of a suspended SiN membrane. AlN is an important material for the emerging field of quantum technologies, especially when photonic integrated circuits with nonlinear optics or optomechanics are involved [9-11]. Due to the used geometry of the membranes, finite-elements simulations are essential for connecting the measurements to the mechanical properties. These simulations are the main focus of this work. The samples and setup are described in Section 0. Section 0 briefly states the experimental outcomes; the simulations are the topic of Section 4. Using these Section 0 gives the resulting extracted stress in the AlN films.

2. Samples and Setup

2.1. Nanofabrication, AlN Growth and Chip Layout

Our membranes are made on chips with a 330 nm thick stoichiometric SiN layer, which is grown commercially on top of a 3.17 um thick silicon oxide (SiOx) layer using LPCVD and has a tensile stress of about 1100 MPa. Underneath these two layers is the silicon carrier. Release holes are defined in the silicon nitride using electron-beam or optical lithography followed by reactive ion etching. The number of holes and their spacing set the size of the membrane. For this work, a single layout was used with 120 membranes with varying size on every chip, as shown in Fig. 1. The holes in the SiN layer expose the underlying oxide and by immersing the chip into buffered hydrofluoric acid (BHF), the exposed SiOx is etched isotropically, resulting in circularly expanding drums originating at the etch holes. The etching is continued until these "drums" are no longer supported by "pillars", thus forming a fully suspended SiN membrane. The radius of the drums R is the sum of the radius of the etch hole and the underetching distance. The finite selectivity of BHF between SiN and SiOx (~1:71) results in a uniform thinning of the top surface and slightly tapered bottom profiles of the SiN. The tapering originated from the duration a specific part was exposed to the etchant. It thus tapers from the same amount as removed from the top side at the release hole, to zero at the end of the drum, i.e. at $r = R$. This is also visible in optical reflection maps.

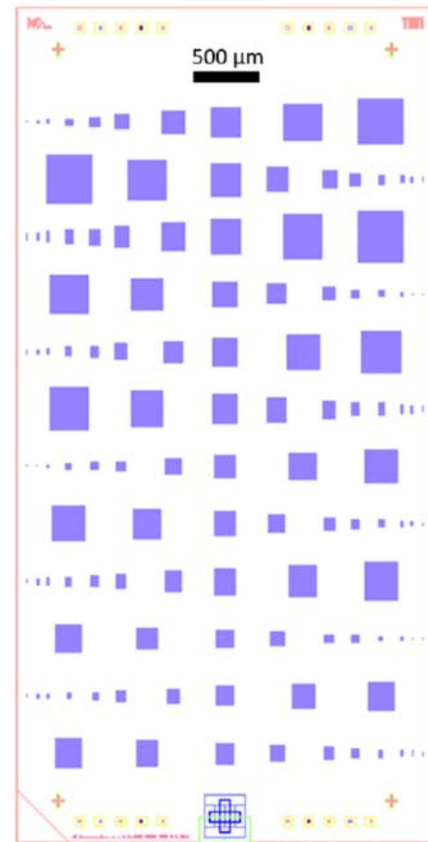

Fig. 1. Layout for a 6×10 mm chip with 120 membranes of different sizes indicated in blue. Structures for alignment, device and chip identification, and logos are indicated in red. Marker protection using SU8 is shown in yellow.

The resulting "silicon-nitride only" membranes can already be used for a variety of optomechanical experiments. In particular we have used these to demonstrate efficient mode mapping [3] – even in the presence of crosstalk [12] – and to study the spatial structure of nonlinearities.

However, here as the next step, AlN is grown on top of the membranes using DC magnetron sputtering using the process that we developed for hybrid photonic integrated circuits and which is detailed in [13]. Using X-ray diffraction, it was confirmed that these films are of good crystalline quality and have a strong c-axis orientation. Also, optical reflectometry indicates that the films have low optical losses. In addition, atomic force microscopy shows low roughness, indicating that the films are of good quality. However, accessing the mechanical properties is more difficult, and hence an important open task. For example, it is known from literature that the growth process and the final thickness influence the stress in the AlN [14]. It is thus important to have a quick and reliable method to determine the stress in the deposited film and in the resulting bi-layer membrane. Our other work [8], we will focus on the measurements and outcomes, whereas here the focus in on the more technical results, in particular on the implementation of the finite element simulations. However, before focusing on that topic, first the setup

and kind of results that are obtained are discussed to give the reader a good idea of the important aspects of the simulations.

2.2. Experimental Setup

The chips are glued onto a piezo element for actuation and mounted in a vacuum chamber as shown in Fig. 2.

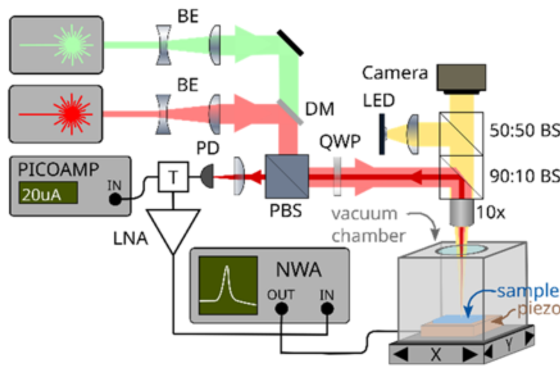

Fig. 2. Schematic of the measurement setup. Two different lasers can be used for measuring the driven response of the bilayer membranes that are mounted on a piezo actuator and placed in the vacuum chamber. For clarity, the green laser light path is not shown in full. Adapted from [3].

In short, a red HeNe laser (633 nm, Mellers Griot 05-LHP-141) is focused onto one of the membranes – or any other mechanical resonator – using a long-working-distance objective (Mitutoyo M plan apo 10x) that is located outside the vacuum chamber. The reflected light is collected via the same objective and focused onto a high-speed photodetector (Newport 818-BB-21). Since the reflection depends on the distance between the membrane and the highly reflecting Si, this provides a sensitive way to measure the local displacement of the membrane [3]. The driven response is measured using a network analyzer (HP 4396A). Typically, first overview scans are acquired and then zooms of the resonances are taken at higher resolution. From the resonance peaks, the eigenfrequencies and quality factors are obtained by fitting a harmonic oscillator (or Duffing) response to the data. This procedure is repeated semi-automatically for the different membranes on each chip. Then the next chip with a different AlN thickness is inserted and measured again, resulting in large datasets that are processed using MATLAB® scripts. Using these, the responses can be viewed, fitted, and the fit results can be studied as function of the membrane parameters. Fig. 3 shows a selection of four membranes with identical size on the four different chips. The peaks correspond to the fundamental (i.e., the (1,1) mode [3]) out of plane eigenmodes. A clear dependence on the AlN thickness can be seen: the thicker the AlN, the lower the resonance frequency. Here it is noted that in the overviews, the driving power is relatively high and that the peaks appear somewhat distorted, but care is taken to measure the zooms of the resonances with enough resolution and low enough excitation so that the frequencies can be determined precisely from the linear response (or slightly nonlinear response; in that case a Duffing-response fit is used).

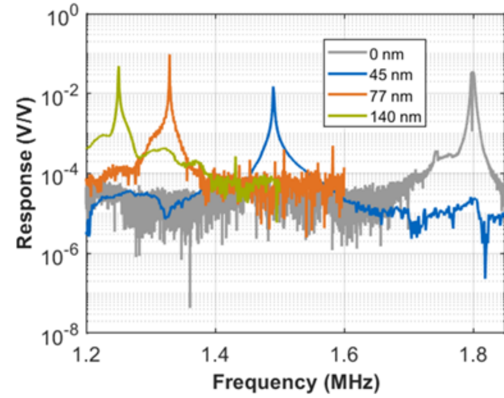

Fig. 3. Driven response near the fundamental eigenfrequency for the nominally-same membrane on different chips with different AlN thicknesses. The AlN layer clearly shifts the resonances to lower frequencies.

The readout always works well for SiN-only membranes, but for bilayer membranes with different AlN thicknesses it is possible that the derivative of the reflectivity with respect to the displacement vanishes. Hence, alternatively a green (532 nm; OneFive Katana) and even a violet laser (405 nm, not shown) can be used to sense the motion. Fig. 4 compares reflectivity maps for two laser wavelengths and two chips with different AlN thicknesses. The differences in contrast between the membrane and support are clearly visible. The different lasers (see Fig. 2) allow selection of the best color for the optomechanical readout. Also note how the small conical tapering of the membrane bottom is clearly visible in these reflection maps.

3. Resonance Frequencies

The driven response is measured for all 480 membranes (120 membranes with varying size per chip as shown in Fig. 1; 4 chips with different thicknesses t_{AlN}). The fundamental eigenfrequencies of the same membrane on four different chips were plotted in Fig. 3; from zooms the exact resonance frequency is determined and this is plotted against the size of the membrane in Fig. 5. The strong variation of the frequency with membrane size makes it beneficial to convert the frequency to the speed of sound for the flexural vibrations, which – for an idealized membrane – equals the square root of the thickness-weighted sum

of the stress and mass density of the bilayer. Specifically, the effective membrane size is given by:

$$L_{\mathrm{eff}} = \left(\frac{1}{L_x^2} + \frac{1}{L_y^2}\right)^{-1/2}$$

This means that L_{eff} tends to the smallest of the two side lengths, that is when $L_x \gg L_y$, L_{eff} equals L_y and vice versa. For a square membrane $L_x = L_y$, and $L_{\mathrm{eff}} = L_x/\sqrt{2}$. The question what the exact side length is when the membrane consists of individual drums, will be addressed in Section 4.3. However, the bottom line is that $2L_{\mathrm{eff}} f_{(1,1)}$ equals the speed of sound *c*. The speed of sound is thus a central quantity that can be determined from the experiments, calculated analytically, and also simulated [8][8]. It contains the material properties of the bilayer, specifically the stresses in the two materials. Hence, with the known properties of the SiN layer, the stress in the AlN film can be extracted. In practice, the membrane has a complex geometry [8, 15]. This means that for the required precision, finite element simulations are used to connect the speed of sound to the material properties, in particular the thickness dependence of the stress in the AlN thin film. This will be detailed in the following section (Section 4).

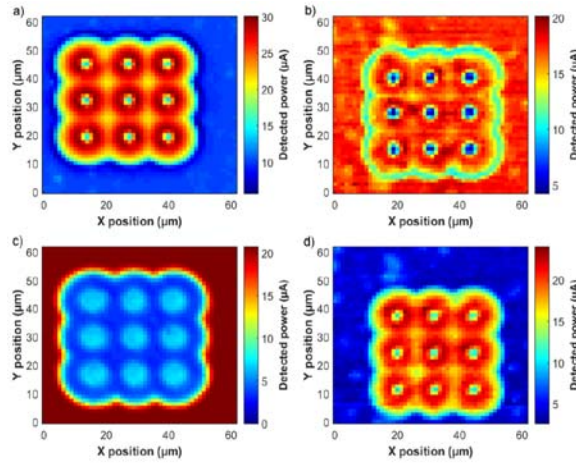

Fig. 4. Reflectivity maps for a 3×3 membrane. The top (bottom) row is taken at 633 (532) nm. The left (right) column has 77 (140) nm of AlN grown onto the suspended silicon nitride membrane [7].

4. Finite Element Simulations

In this section, we describe how the finite-element simulations for connecting the experimentally determined quantities to the parameters of the top layer. Like for the simulations of our stressed pre-displaced string resonators [16] also here the FEM simulations of our structures were initially built with the graphic user interface of COMSOL MULTIPHYSICS® (versions 5.3 to 5.6 were used throughout the project). To sweep parameters, and to extract and process results, the simulations were controlled with our simulation framework written in MATLAB®. For this integration, the COMSOL model was exported as a script and edited to the specific needs. Then the scrips were run via the COMSOL's LiveLink for MATLAB™ on regular personal computers (PCs) with Windows 10. Most of the simulation in this paper were run on a PC with 32 GB memory and an Intel® i7 13700 processor.

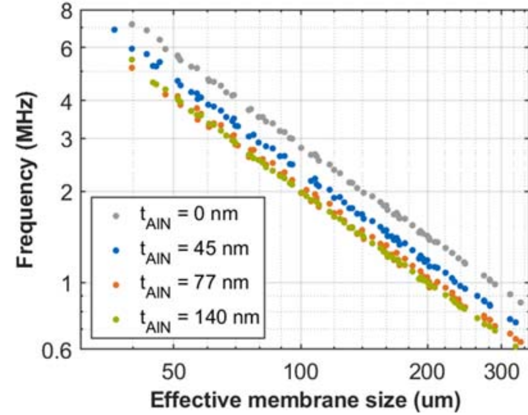

Fig. 5. Measured fundamental resonance frequency f(1,1) for membranes of different size with different amounts of AlN on top. The slope of -1 in this log-log plot indicates that f(1,1) ∝ 1/Leff i.e. that the membranes are stress dominated. Their slope is twice the speed of sound.

4.1. Building the Model

As a first step, the geometry is defined (i.e. a bilayer rectangular membrane, membranes composed of drums, or an individual drum/unit cell, depending on the exact simulation as will be discussed in the next Sections) and Si_3N_4 from the material library is applied to the bottom layer. For the top layer – i.e. the AlN – the mechanical properties are set manually.

Next, the film stresses are added via the initial stress and strain under *linear elastic material* by setting $\sigma_{xx} = \sigma_{yy} = 1105.1$ MPa and $\sigma_{zz} = 0$ for the SiN [16]. The stress in the AlN is set similarly and is varied as a parameter passed by the MATLAB control script. For the full simulations (Sections 4.2 and 4.3), the boundary conditions for the sides are set to the *fixed constraint*. For the band structure simulations (Sections 4.4-4.6) these are set to *symmetric* for the static simulation and *period boundary conditions* are used to find the eigenmodes. Specifically, the *Floquet periodicity* boundary conditions are used and the x and y component of the wavevector **k** are specified: k_x, k_y.

The next step is to build the mesh and different coursenesses can be set. Besides the geometric and material properties, also the mesh coarseness is controlled by the simulation framework so that the influence of the mesh can be studied in detail (see e.g. Section 4.5). In general, one can expect that a finer mesh gives more accurate results at the expense of

longer runtime and memory usage. After the model is set up, it can be solved. This has two steps: First, the stationary solver is used to obtain the relaxed structure, followed by the eigenfrequency solver. One thus has access to both the results from the static relaxation (deformation, stresses), as well as for the dynamics around this relaxed geometry (eigenfrequency, modal displacement, …).

4.2. Full Simulations

The better the simulations reflect reality, the better the agreement should be – at least in principle as there is often a trade-off between detail level, accuracy, and the required computation resources. Still, it makes sense to first see what a full simulation gives. Fig. 6 shows the calculated fundamental frequency $f_{(1,1)}$ of rectangular SiN-only membranes with varying aspect ratios, i.e. ratios between their length L_x and width L_y. For large sizes – say, $L_{eff} > 100$ µm – the membranes are tension dominated and when using the effective length defined above, the frequency in this domain is fully described by the speed of sound.

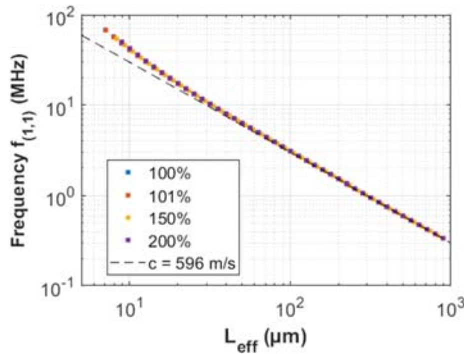

Fig. 6. Simulated fundamental resonance frequency of ideal rectangular SiN-only membranes of different sizes and aspect ratios Lx/Ly. After converting the sizes to the effective length, all curves collapse onto a single line. For large membranes, this matches the frequency calculated for a membrane under tension with a constant speed of sound $c = \sqrt{\sigma/\rho}$ (dashed line). The thickness of the silicon nitride is 330 nm in these simulations.

The next step is to see the influence of the AlN layer on top. Similar to the experimental observations of Fig. 3, Fig. 7 shows that when the thickness of the top layer increased, the speed of sound in the tension-dominated range decreases – and, thus, $f_{(1,1)}$ with it.

This is can be seen in two different ways (note that the mass density of SiN and AlN are very similar):

1. The mass per unit area (in kg/m^2) of the membrane increases with the same amount of tension (in N/m);
2. The mass density (in kg/m^3) remains similar, but the average stress (in N/m^2) decreases.

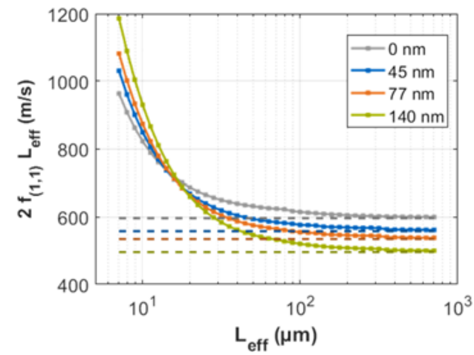

Fig. 7. Simulated frequencies for the fundamental mode multiplied by twice the effective size of square membranes with varying size. The dashed lines indicate the speed of sound as thickness-weighted average of the two layers. colors indicate the different thicknesses of the top layer. In this simulation the thickness of the silicon nitride is 330 nm and the stress of the AlN is 0.

Both ways are understood from a simplified model where the speed of sound is the thickness-weighted average of the density and stress in the two layers [8]. The simulations converge to this value (dashed lines) for large effective sizes. Also visible is that the crossover to the bending regime moves to slightly larger membranes for thicker AlN as the bending rigidity is proportional to the total thickness to the power 3 [17]. There, the thickest layer of 140 nm also has the highest speed of sound. We note again that the actual structure of our membranes is more complex than a simple uniform rectangular membrane. In particular:

1. There are periodically arranges etch holes in the SiN, where the in-plane stress can partly relax;
2. The finite selectivity partly removed the SiN, resulting in cone-like structures at the bottom. The thickness of SiN is thus reduced below the initial nominal value of 330 nm and varies with the location;
3. The fact that the membrane constitutes of individual drums implies that the sides have “wavy” instead of straight edges.

Full simulations of small membranes taking all these elements into account are feasible, but for larger sizes this soon results in excessive simulations duration or required resources as shown in Fig. 8. Membranes with thin AlN layers and all features take the longest; simple SiN-only membranes (dark blue color) are the fastest (e.g. when simulating the results for Fig. 6 and Fig. 7) as there are no small features in the plane. Still, the simulation time increases roughly exponentially with the drum number. This means that simplifications have to be made. We will first address the third point in the next section (4.3) and with the findings there, it is shown that the other two points can be tackled using band structure simulations (Section 4.4). Note that for membranes made from a small number of drums the modes may be different from the modes of a rectangular membrane under tension, where: $u_{m,n}(x,y) \propto \sin(\pi m x/L_x)\sin(\pi n y/L_y)$ [3].

In particular for $N_x = N_y = 1$ the membrane is just a single circular drum where – in the tension dominated case – the eigenmodes are given by Bessel functions instead of sine functions [18]. There it is commonplace to also label the modes with two integers in round brackets, giving the number of nodes in the angular and antinodes in the radial direction, respectively. In the following we usually label the modes with a single number i that indicates the ordering. f_1 is thus the lowest (i.e. fundamental) mode of every membrane and would correspond to $f_{(1,1)}$ for a rectangular membrane and $f_{(0,1)}$ of a circular one.

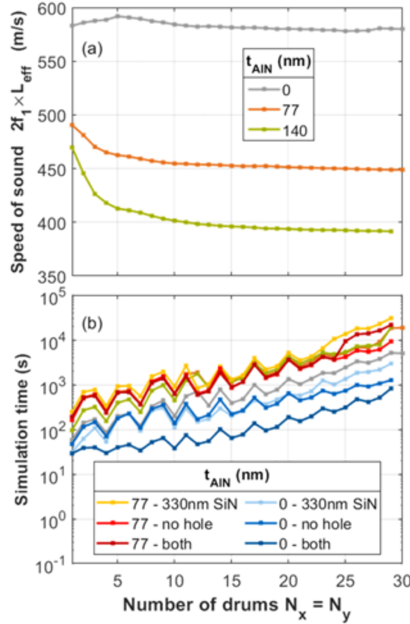

Fig. 8. Full simulations of membranes with varying number of drums. (a) shows the duration of each simulation. (b) Speed of sound for three different thicknesses. The other lines in (a) show the influence of several features, such as no removal of SiN, no release hole or both. The order of the simulations varied, resulting in a wavy pattern. $R = 11$ µm and $A = 14.56$ µm. 330 nm SiN with 140 nm removed unless mentioned otherwise.

4.3. Influence of the Drums at the Edges and Corners

As can be seen in e.g. the reflection maps from Fig. 4, the outline of the membranes is not a perfect rectangle as it is made from a discrete number of overlapping drums. The impact of this is studied using simulations in this Section. For this, pure silicon nitride membranes without etch holes are simulated. The thickness was kept constant at 330 nm, so that the impact of the other two points from Section 4.2 do not play a role and the edge effects can be isolated. Fig. 9(a) shows the simulated fundamental resonance frequency where the outer dimensions $L_x = L_y$ were kept fixed, but the number of holes was varied (keeping $N_x = N_y$). Since $L_{x,y} = 2R + (N_{x,y} -1)A_{x,y}$ this means that the lattice constants $A = A_x = A_y$ thus varied with the number of drums to keep the size the same. The overlap $2R – A$ thus increased and the insets show that the larger the number of drums, the smoother the edges appear. The simulated frequencies are higher for small numbers and tend to a limiting value for large numbers. Note that for $N_x < 12$, the membrane would not be fully suspended as $A_x^2+A_y^2 > 4R^2$, i.e. that the aforementioned "pillars" remain. Hence these points are not included in the plot. The solid lines indicate the frequency estimated using the speed of sound $c = \sqrt{\sigma/\rho}$. In this case, either the outside (red), or the inner side (green) length is taken to calculate the effective membrane size. In the latter case one obtains:

$$L_{\text{eff}} = \left(\frac{1}{(L_x - 2\Delta L_x)^2} + \frac{1}{(L_y - 2\Delta L_y)^2}\right)^{-1/2},$$

where $\Delta L_{x,y} = R - \sqrt{(R^2 - A_{y,x}^2/4)}$. It is clear that the corrected effective size describes the increase with reduced drum number reasonably well. The small offset of about 50 kHz is attributed to the remaining bending rigidity of the flat 330 nm-thick membrane. This shows that irrespective of the "wavy" edges, the frequency is still given by $c/2L_{\text{eff}}$ as long as the right dimensions are used in the analysis. Still, the finite radius of the drum in the four corners may also influence the results. This is studied in **Error! Reference source not found.**(b).

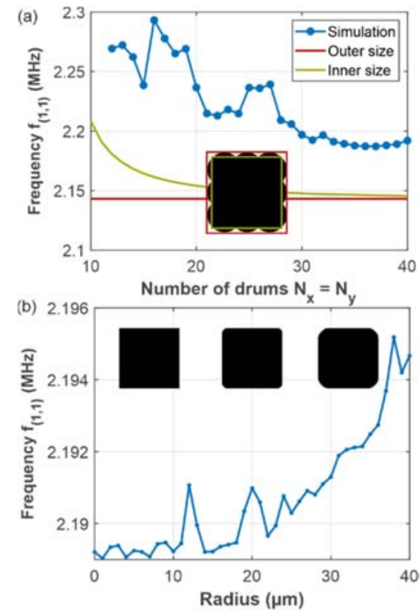

Fig. 9. Simulated fundamental frequency of SiN-only membranes consisting of an Nx × Ny array of drums (a). The drum radius was 11 µm, but etch holes were not included as explained in the text. The solid lines show the frequency estimated using the speed of sound and the effective length determined from the outer size (red) and the inner size of the membrane (green) as shown schematically in the inset. (b) Rectangular membrane with rounded corners as illustrated in the insets. In all simulations in this figure, the outer side length was kept at 196.7 µm.

Here, again 330 nm flat SiN-only membranes without etch holes are simulated. Now, the edges are kept straight, but the corners have a varying "fillet" radius R. A perfect rectangular membrane would have $R = 0$, but experimentally, we have $R = 11$ μm (1 μm due to the release hole, plus 10 μm due to the lateral etching). Fig. 8(b) shows that in this case, the correction is very small (~10^{-4}). This thus shows that the effect of the non-straight edges and corner radius can thus be neglected in the experimentally-relevant geometries.

Finally, it was found that the *virtual operation* to ignore the internal boundaries between the overlapping drums when meshing the structure resulted in a significant speedup, without which the simulations in this Section would have taken unreasonably long.

4.4. Unit Cells vs Full Simulations

As we argue in [8], the fact that the membranes consist of periodically-repeating structures of etch holes and "cones" due to the nonuniform etching of the bottom side where the etch holes are located at a square lattice means that an infinitely large membrane can be described fully using band structure calculations of individual unit cells. Although we showed in Section 4.3 that the edges do not significantly impact the resulting eigenmodes – at least not when using the correct dimensions, it is not a priory clear if the band structure calculations can also be used to accurately model membranes of finite size.

In this case, the speed of sound is given by ω_i/k which becomes $c = 2f_1 \times \pi/k$ for the fundamental mode. This relation connects the magnitude of **k**, i.e. k, to effective size of the membrane $L_{\text{eff}} = \pi/k$. Although it was shown in [8] that the direction of **k** is not relevant for the fundamental mode – a statement that will be discussed further in the next section, this could be taken into account by evaluating the frequencies for $k_x = \pi/L_x$ and $k_y = \pi/L_y$. However, this would imply that again every membrane geometry has to be simulated. Right now, only a single value for **k** suffices for each unit cell (corresponding to 30 membrane), significantly speeding up sweeps of parameters (e.g. the AlN film stress in Section 4.6).

The results are presented in Fig. 10. In comparison to the full simulations, there is a clear deviation at small sizes, where the bending rigidity becomes apparent. Although the bending of the unit cell itself is taken into account (causing the increase at very small L_{eff}), this is not true for the bending due to the clamping at the edges as the band structure calculations assume an infinitely extending lattice. Still for large membranes this should not too important and both the full and unit cell simulations show – a slightly different – converging value. Future work will need to determine the origin of this shift of a few m/s. Interestingly, the unit cell simulations do approach the value $\sqrt{\sigma_{avg}/\rho_{avg}}$ so the deviation is more likely to be in the full simulations instead of the unit cell ones. A technical point is that for the "ideal" SiN-only and square membrane with AlN there is no true periodicity (it is a uniform rectangle) so that one is free to impose any value (here, also $A = 14.56$ μm is taken), a bit in analogy to the empty lattice calculations of free-electron band structures in solid state physics [19]. Note that the single full simulation (gold) at $L_{\text{eff}} \sim 300$ μm took more than 5h to complete (same data as the orange curves in Fig. 8) whereas for the unit cells it was only about 3 min.

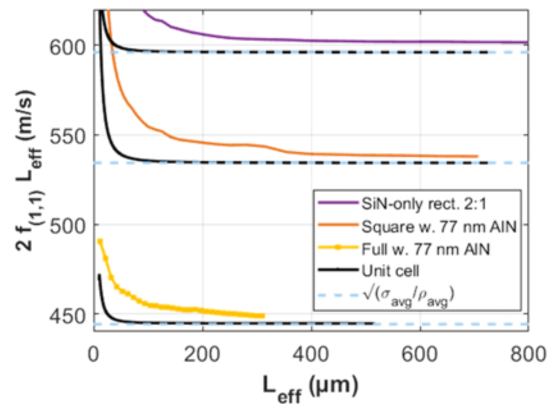

Fig. 10. Speed of sound calculated using unit cells compared to full simulations in three cases: a rectangular SiN-only membrane (cf. Fig. 6), a square membrane with 77 nm AlN and 330 nm SiN and a full membrane with 77 nm AlN (cf. Fig. 8). For large sizes, the curves approach a constant value, which for the unit cell calculations coincides with the respective values of $\sqrt{\sigma_{avg}/\rho_{avg}}$ (dashed lines).

4.5. Role of Clamping and Global Constraint

For the full simulations (Sections 4.2 and 4.3), it is clear what the boundary conditions are. However, for an infinitely repeating unit cell, the periodic boundary conditions for the static solution imply that the any solution plus a uniform displacement is still a solution and an error is raised when running the simulation. Thus, there must be an additional constraint to fix the overall displacement. For this, an "anchor" point at the rim of the etch hole is set to zero displacement for the static simulation. This additional constraint is disabled when running the eigenmode solver as there the Floquet boundary conditions remove the ambiguity in the solution. Fig. 11 shows the influence of the anchor point on the resulting first three eigenfrequencies. Note that the unit cell belongs to the C_{4v} point group and that the frequencies should thus be periodic every 90 deg. when varying the direction of **k**. Any pure 180-deg. periodicity signifies a difference between X and Y that is not present in the geometry and must thus be due to the artificial additional constraint.

The second eigenmode f_2 – a transverse mode – shows a very pronounced 90° periodicity, without any sign of pure 180° components. Changing the location of the anchor does not give different frequencies (the blue curve is hidden underneath the orange one). This

mode thus depends on propagation the but does not "feel" the anchor. The situation is reversed for the fundamental mode. Here there is a clear pure 180º trend that flips with a change in the anchor position, both are a clear indication of the influence of the anchoring. Still, the mode itself does not depend on the direction of the wavevector **k**. Moreover, even though there is an effect visible, the difference between the two curves for f_1 is only 0.21 % so this is negligible in practice. As an alternative it is also possible to apply global "weak" constraints, e.g. that the displacement averaged over the entire geometry is zero. However, as shown in Fig. 12, this does results in a huge increase in the computation time, without any significant change in the final frequency. Hence the anchor (at the location of the blue point) will be used in the following.

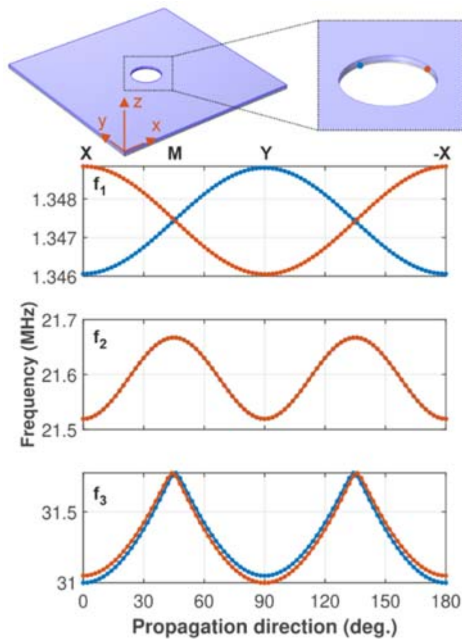

Fig. 11. Influence of the anchoring point for the static simulation of the unit cell. First three eigenfrequencies for different directions of the wavevector **k**. Its magnitude was k = 2.24×10^4 m^{-1} = 0.104 π/A. The blue and orange curves are for anchoring points as indicated with the same colors in the inset top panel.

4.6. Stress Distribution

Now that the validity of the simulations has been verified, a closer look at the outcomes can be taken. Of course, the main interest are the frequencies, from which the speed of sound can be obtained $c = 2f_i \times \pi/k$. Then this can be done while varying parameters of the unit cell (AlN thickness, lattice constant, …) and material properties – in particular σ_{AlN}. This can then be used to determine the latter from the experimental observations [8] as will be summarized in Section 5. Still the simulations allow access to other quantities that are not easily accessible in the experiment, in particular the stress tensor components and their distribution throughout the structure (cf. bilayer unit cell). To illustrate this, we simulated the static relaxation of a typical unit cell and show the results in Fig. 13 and Table 1.

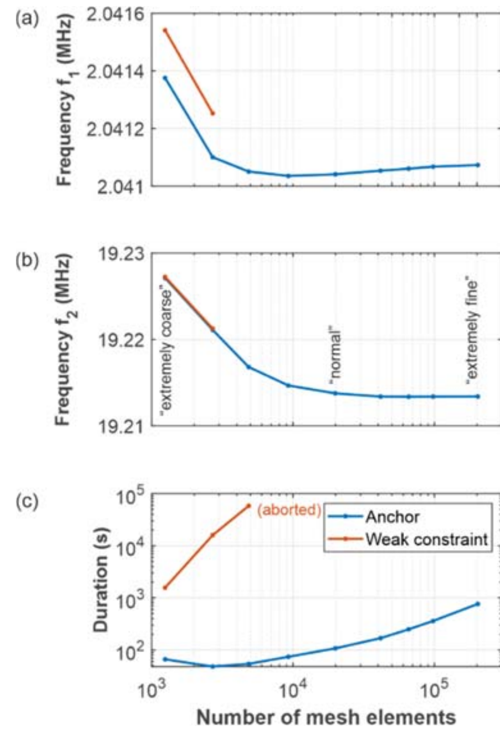

Fig. 12. (a, b) Evolution of the frequency of the first two modes and simulation time (c) for different fineness of the mesh. In the COMSOL GUI these correspond to the choices between "extremely coarse" and "extremely fine" as indicated in (b). In every panel, the two curves correspond to the anchoring (blue) and weak constraint (orange) method as detailed in Section 4.5. The latter is much slower and shows a worse scaling with number of elements, whereas there is no significant change in the final frequency. Note the very small relative span in (a) and (b). Simulation w/o AlN.

Table 1 shows the different cartesian elements of the stress tensor σ_{ij} averaged over the different parts of the membrane. It is clear that both the z (i, j = 3) and shear components (I ≠ j) remain small. Also, the stresses remain largely isotropic and that there only a small amount of relaxation from the initial values for the film stresses took place. Given this, we focus on the principal stresses $\sigma_{1,2,3}$ (i.e. the ordered eigenvalues of the matrix that represents the stress tensor in a fixed coordinate system, where σ_1 is the largest [20]) instead of the cartesian components as these will better reflect the symmetries of the structure. The first two are visualized in Fig. 13. Interestingly, the anchoring point shows a larger stress, but from the discussion in Section 4.5 it is clear that this does not influence the results. Overall, one can see that at the bottom of the

SiN layer, the stress is slightly reduced as the cone-like removal of the SiN starts at the etch hole in the center leaving slightly thicker protrusions at the corners where the stress can somewhat relax (orange). This nonuniform stress leads to a ~100 nm downward bending of the membranes at the location of the holes. It would be interesting to see if this is the reason of the gradient of the optical reflectivity near the holes (see e.g. Fig. 4), that this is due to the tapered thickness profile, because of optical effects due to the finite spot size and/or depth of focus of the setup, or a combination thereof.

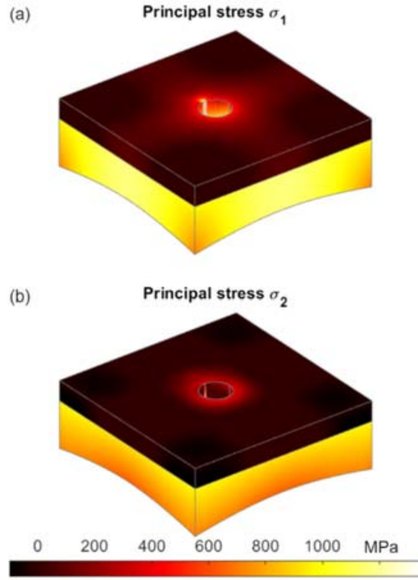

Fig. 13. Distribution of the stress after relaxation (static simulation) throughout the unit cell with A = 14.56 µm. The original SiN thickness of 330 nm is reduced by 140 nm from the top and bottom (conical) and the top layer is 77 nm of AlN. The initial film stresses were 1101.5 MPa for SiN and 0 MPa for AlN. The z axis is scaled 10× for visibility. Panels (a) and (b) show the first and second principal stress, respectively. Note that $\sigma_3 \sim \sigma_{33} \sim 0$).

Table 1. Elements of the stress tensor averaged over the bottom layer (SiN), the top layer (77 nm AlN) or over the entire unit cell after the static relaxation from the simulation shown in Fig.. The initial film stresses were 1101.5 and 0 for SiN and AlN, respectively. All stresses are given in MPa and rounded.

	σ_{11}	σ_{22}	σ_{33}	σ_{23}	σ_{13}	σ_{12}
SiN	1045	1048	0	0	0	0
AlN	-6	-3	0	0	0	0
Avg.	624	627	0	0	0	0

Finally, the influence of the film stress is studies as is shown in Fig. 14. As expected, the average stress in the membrane increases when the stress in the AlN film increases. There is also a dependence of the lattice constant. The smaller A, the lower the average stress. In this case, more SiN is removed as the overlap is larger and also the impact of the holes, where the stress can partly relax, becomes stronger. This trend is also visible in the calculated speed of sound. Over the whole parameter range, the speed of sound is accurately represented by the square root of the final average stress and the density (dashed lines). These simulations can then be repeated for different AlN thicknesses and then compared to the experimental observations.

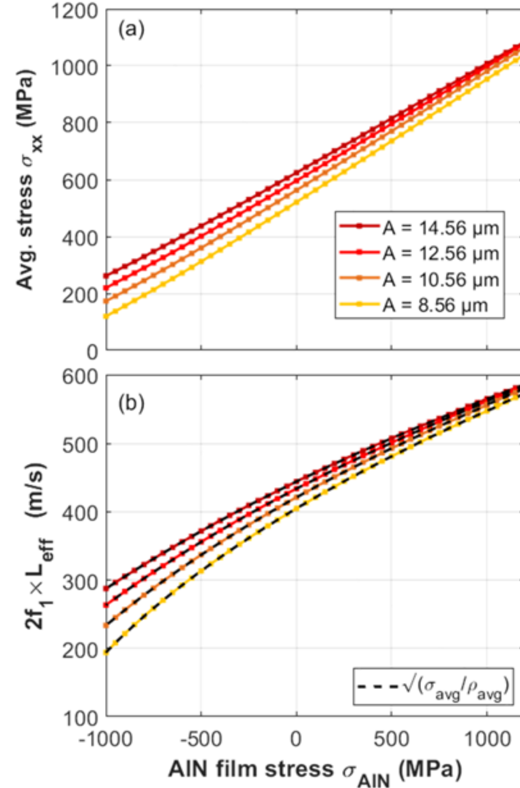

Fig. 1. Dependence of (a) the average in-plane stress (only σ_{xx} is plotted; σ_{yy} is indistinguishable) and (b) speed of sound for varying AlN films stresses. The different colors indicate the different lattice constants used in the experiments. The dashed lines give the predicted c based on the average stress (xx component as in (a)) and density (mass of the unit cell divided by its volume). The AlN thickness was 77 nm and 140 nm of the 330 nm SiN was removed.

5. Thickness Dependence of the AlN Film Stress

The data in Figs. 3 and 5 showed a clear dependence on of the resonance frequencies on the AlN thickness and with the finite element simulations that were described in detail in the previous section, this can be now analyzed quantitatively. The analysis is described in detail in [8][8], but here the final results are presented. Fig. 15 shows the stress in the AlN thin film as a function of the thickness. Interestingly, it shows that the stress transitions from compressive to tensile. We believe that this is due to the complex growth of AlN on SiN [7] and a finer sweep of the film thickness will be done to study this in more detail.

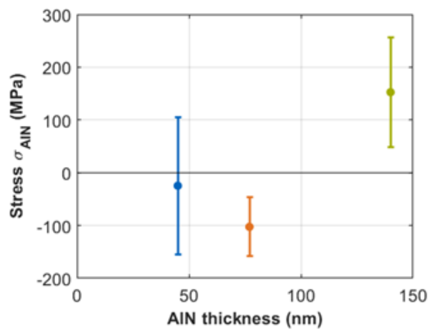

Fig. 15. Extracted stress in the AlN film σ_{AlN} vs the thickness t_{AlN}. The errorbars are represent the fit uncertainty as returned by MATLAB's `fit` function.

6. Conclusions and Outlook

As proof of principle, we have used our SiN micromechanical membranes to determine the stress in AlN thin films that were grown on top. Finite element simulations are essential to connect the measured resonance frequencies to the mechanical properties of the membranes. The reason is that the membranes are more complex than a perfect rectangular membrane under tension. The used geometry, however, has the benefit of simple interferometric readout of the motion. It is shown that full simulations are very expensive so simplifications have to be made. It is shown that the wavy edges and rounded corners do not play an important role, at least not when the right dimensions are used for the effective length. The release hole and conical profile can be captured by band structure calculations. For the static relaxation, the role of an additional anchoring point vs a global constraint is studied. The latter – although more reflecting reality – did not improve the results, and resulted in a dramatic increase of the computation time. With the verified simulations, the stress distribution and dependence on the film stress were studied. This allowed extraction of the stress in the AlN from the experimental data. Although here we focused on AlN, our method is not limited to this material, as in principle any (semi-) transparent material may be sensed. With slight changes to the optical setup (specifically: heterodyne detection), even that requirement may be lifted in the future. The method is thus applicable to any transparent or reflecting thin film that can be grown onto our suspended SiN membranes. Further improvements will include damping and also smaller structures so that besides the stress also other mechanical properties such as the Young's modulus can be determined. Also here, we expect a strong synergy between the experiments and the finite-element simulations.

Acknowledgements

We thank Aditya and J. Röwe for measurements, T. Sommer, A. Zinth and M. Althammer for discussion, D. Hoch and J. Röwe for assistance with nanofabrication, and M. Müller for growth of the AlN.

Funding: DFG EXC-2111-390814868 and TUM-IAS (DFG & EU FP7 291763).

References

[1]. D. Hälg, T. Gisler, Y. Tsaturyan, L. Catalini, U. Grob, M.-D. Krass, M. Héritier, H. Mattiat, A.-K. Thamm, R. Schirhagl, E. C. Langman, A. Schliesser, C. L. Degen, A. Eichler, Membrane-Based Scanning Force Microscopy, *Phys. Rev. Appl.*, Vol. 15, Issue 2, February 2021, L021001.

[2]. J. D. Thompson, B. M. Zwickl, A. M. Jayich, F. Marquardt, S. M. Girvin, J. G. E. Harris, Strong dispersive coupling of a high-finesse cavity to a micromechanical membrane, *Nature*, Vol. 452, March 2008, pp. 72-75.

[3]. D. Hoch, K.-J. Haas, L. Moller, T. Sommer, P. Soubelet, J. J. Finley, M. Poot, Efficient Optomechanical Mode-Shape Mapping of Micromechanical Devices, *Micromachines*, Vol. 12, July 2021, 880.

[4]. H. Xu, D. Mason, L. Jiang, J. G. E. Harris, Topological energy transfer in an optomechanical system with exceptional points, *Nature*, Vol. 537, 2016, pp. 80-83.

[5]. K. Y. Fong, H.-K. Li, R. Zhao, S. Yang, Y. Wang, X. Zhang, Phonon heat transfer across a vacuum through quantum fluctuations, *Nature*, Vol. 576, 2019, pp. 243-247.

[6]. P.-L. Yu, T. P. Purdy, C. A. Regal, Control of Material Damping in High-Q Membrane Microresonators, *Phys. Rev. Lett.*, Vol. 108, Issue 8, February 2012, 083603.

[7]. A. Yadav, T. Sommer, M. Althammer, M. Poot, Sensing the mechanical properties of AlN thin films using micromechanical membranes, in *Proceedings of the 9th International Conference on Sensors Engineering and Electronics Instrumentation Advances (SEIA'23)*, Portugal, 2023, pp. 90-93.

[8]. T. Sommer, Aditya, R. Gross, M. Althammer, M. Poot, Determining the mechanical properties of AlN films using micromechanical membranes, 2023, in preparation.

[9]. G. Terrasanta, T. Sommer, M. Müller, M. Althammer, R. Gross, M. Poot, Aluminum nitride integration on silicon nitride photonic circuits: a hybrid approach towards on-chip nonlinear optics, *Optics Express*, Vol. 30, March 2022, pp. 8537-8549.

[10]. X. Liu, A. W. Bruch, H. X. Tang, Aluminum nitride photonic integrated circuits: from piezo-optomechanics to nonlinear optics, *Adv. Opt. Photon.*, Vol. 15, March 2023, pp. 236-317.

[11]. L. Fan, C.-L. Zou, M. Poot, R. Cheng, X. Guo, X. Han, H. X. Tang, Integrated optomechanical single-photon frequency shifter, *Nat. Photon.*, Vol. 10, Dec. 2016., pp. 766-770

[12]. T. Sommer, D. Hoch, K.-J. Haas, L. Moller, J. Röwe, A. Yadav, P. Soubelet, J. J. Finley, M. Poot, Optomechanical mode-shape mapping in the presence of crosstalk, *Sensors & Transducers*, Vol. 256, July 2022, pp. 1-9.

[13]. G. Terrasanta, M. Müller, T. Sommer, S. Geprägs, R. Gross, M. Althammer, M. Poot, Growth of aluminum nitride on a silicon nitride substrate for hybrid photonic circuits, *Materials for Quantum Technology*, Vol. 1, June 2021, 021002.

[14]. L. Xie, H. Zhang, X. Xie, E. Wang, X. Lin, Y. Song, G. Liu, G. Chen, Structure and Optical Properties of AlN Crystals Grown by Metal Nitride Vapor Phase Epitaxy with Different V/III Ratios, *ACS Omega*, Vol. 7, July 2022, pp. 23497-23502.

[15]. V. P. Adiga, B. Ilic, R. A. Barton, I. Wilson-Rae, H. G. Craighead, J. M. Parpia, Modal dependence of dissipation in silicon nitride drum resonators, *Applied Physics Letters*, Vol. 99, 2011, 253103.

[16]. X. Yao, D. Hoch, M. Poot, Relaxation and dynamics of stressed predisplaced string resonators, *Phys. Rev. B*, Vol. 106, Issue 17, November 2022, 174109.

[17]. M. Poot, H. S. J. van der Zant, Mechanical systems in the quantum regime, *Phys. Rep.*, Vol. 511, 2012, pp. 273-335.

[18]. W. A. Strauss, Partial Differential Equations – An Introduction, *John Wiley and Sons Inc.*, 1992.

[19]. C. Kittel, Introduction to Solid State Physics, 8 Ed., *Wiley*, 2004.

[20]. T. J. Chung, Applied Continuum Mechanics, *Cambridge University Press*, 1996.

Published by International Frequency Sensor Association (IFSA) Publishing, S. L., 2023 (http://www.sensorsportal.com).

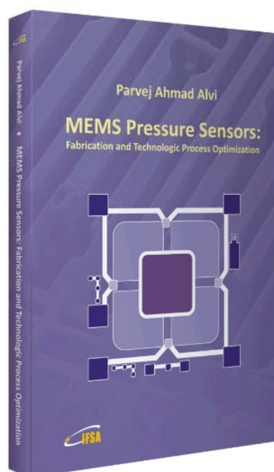

So far, no book has described the step by step fabrication process sequence along with flow chart for fabrication of micro pressure sensors, and therefore, the book has been written taking into account various aspects of fabrication and designing of the pressure sensors as well as fabrication process optimization. A complete experimental detail before and after each step of fabrication of the sensor has also been discussed. This leads to the uniqueness of the book.

Features include:
A complete detail of designing and fabrication of MEMS based pressure sensor.

- Step by step fabrication and process optimization sequence along with flow chart, which is not discussed in other books.
- Description of novel technique (lateral front side etching technique) in terms of chip size reduction and fabrication cost reduction, and comparative study on both the techniques (i.e. Front Side Normal Etching Technology and Front Side Lateral Etching Technology) for the fabrication of thin membrane.
- Discussion on issues of sealing of conical tiny cavity; because the range of pressure applied (i.e. greater or less than atmospheric pressure) can be decided by methodology of sealing of tiny cavity.
- A complete theoretical detail regarding aspects of designing and fabrication, and experimental results before and after each step of fabrication.

MEMS Pressure Sensors: Fabrication and Process Optimization will greatly benefit undergraduate and postgraduate students of MEMS and NEMS courses. Process engineers and technologists in the microelectronics industry including MEMS-based sensors manufacturers.

Hardcover: ISBN 978-84-616-2207-8
e-Book: ISBN 978-84-616-2438-6

Order: http://www.sensorsportal.com/HTML/BOOKSTORE/MEMS_Pressure_Sensors.htm